Heritage Science

RESEARCH Open Access

Reinforced protection of fragile bronze cultural relics based on nano-cuprammonium fiber material

Jinlong Tan[1*], Jiachang Chen[2*] and Xinzhan Cui[3]

Abstract

Bronze artifacts often suffer from "bronze disease" due to the presence of chloride ions, which result from copper chlorides forming on their surfaces during storage. Therefore, reinforced protection is essential for these unearthed cultural artifacts, and new materials for the reinforced protection of fragile bronzes are urgently needed. In this study, cuprammonium solvent and nanocellulose (CNC) were utilized as reinforcement materials to protect fragile bronzes. The chemical and aesthetic properties before and after reinforcement were analyzed using ultra-depth field microscopes, SEM-EDX, XRD, and Raman spectroscopy. The results indicated that at a nano-cuprammonium reinforcer concentration of 2.5 mol/L, the optimal reinforcement effect on simulated bronze powdery rust samples was achieved. Mechanical strength increased by an average of 77.59%. The mass growth rate reached 84.8%, while the color difference ΔE remained below 4.0. Additionally, aging resistance significantly improved, aligning with cultural artifact protection standards.Meanwhile, a compact and stable protective membrane formed on the surface of the bronzes, isolating the bronze matrix from direct contact with the external environment, which delayed bronze corrosion and contributed to long-term stable preservation.

Keywords Bronze disease, Cuprammonium, Nanocellulose, Reinforcement, Cultural relic protection

*Correspondence:
Jinlong Tan
tjlwenwubaohu@gs.zzu.edu.cn
Jiachang Chen
chenjiachangbaohu@163.com
Full list of author information is available at the end of the article

Graphical Abstract

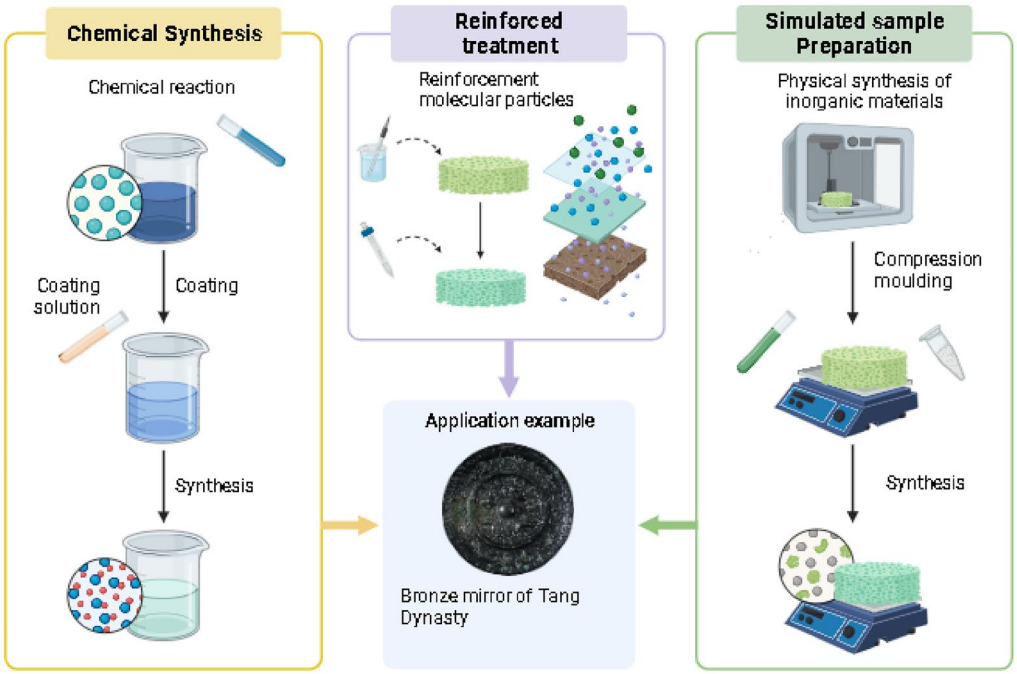

Introduction

Most ancient bronze artifacts in China were unearthed from archaeological sites after remaining buried for long periods of time. These artifacts are prone to various types of corrosion, influenced by environmental factors,such as water, oxygen, soluble salts, and biological matter in the soil [1, 2]. Typically, rust on these artifacts can be classified into three major categories: stable rust, active rust, and harmful rust. Stable rust generally does not damage the underlying bronze substrate and can even augment the artifact's historical value, thus usually requiring no specialized intervention for conservation.Active rust, however, can evolve into harmful rust under favorable conditions, potentially leading to severe degradation of the bronze substrate [3]. Additionally, "powdery rust" can accelerate the corrosion of bronze artifacts when exposed to conducive environmental conditions, threatening not only their artistic value but also their long-term preservation [4–10].

The concept of "Fragile bronze artifacts" is based on subjective perception of the preservation of cultural relics [3]. It is a consequence whereby bronze artifacts lose (or do not possess) their original metal toughness and strength, are easily broken, damaged and difficult to handle by conventional methods. They contain deep mineralization, powdery rust and thin walls. However, there is no consensus in the academic community regarding the definition and criteria for distinguishing fragile bronze artifacts, leading to issues such as multiple connotations and subjectivity [11–13].

"Powdery rust" refers to a bright green, loose, powdery corrosion product found on bronze artifacts containing chlorine. Under suitable conditions, it can spread rapidly and penetrate the bronze matrix, leading to perforation, disintegration, or even the complete collapse of the artifacts. This phenomenon is commonly known as "bronze disease" by researchers. The main chemical component of powdery rust is copper hydroxychloride ($Cu_2(OH)_3Cl$) [14, 15]. This study focuses primarily on the corrosion effects of powdery rust on fragile bronze artifacts.

Current research on the stabilization and protection of fragile bronze artifacts primarily focuses on severe mineralization and the spread of "powdery rust" [16]. Preservation methods commonly used by scholars both domestically and internationally primarily focus on cleaning and rust removal, as well as reinforcement and coating. Common cleaning and rust removal methods for bronze cultural relics include laser rust removal [17], the silver oxide sealing method [18], and low-temperature plasma rust removal, among others [19].

Archaeologically unearthed fragile bronze artifacts often exhibit severe corrosion, fragile textures, cracks,

deformation, significant mineralization, and powdery rust. These artifacts require reinforcement and protection to ensure their long-term stability and preservation.

Epoxy resin is a polymer containing multiple epoxy groups, renowned for its excellent adhesion and toughness. Since the 1960 s, epoxy resin has been extensively used in cultural heritage conservation for bonding and reinforcing various artifacts, including ceramics, bronze, and stone relics. Ma Yu et al. [20] from the Museum of the First Emperor of Qin used E-44 epoxy resin combined with fiberglass cloth (forming fiberglass) to bond and reinforce fractures in a bronze crane from Pit No. 23 of the Emperor Qinshihuang's Mausoleum, restoring appearance of the artifact and overall aesthetics. However, due to the aging phenomenon of epoxy resin, artifacts treated with it may experience discoloration, delamination, and other issues, necessitating further improvement in its aging resistance.

Acrylic resin is a type of polymer synthesized primarily from acrylic esters or methyl methacrylate, characterized by a main chain without unsaturated structures and side chains with ester structures [21]. This structural composition endows acrylic resin with excellent chemical stability, good film-forming properties, and safety in use. The application of acrylic resin in cultural heritage conservation dates back to the 1960 s. In 1968, Italian scholars first used it for the reinforcement and protection of carvings on the door frames of the Siena Cathedral [22]. For over half a century, acrylic resin has been widely used as a reinforcement and protective agent for bronze artifacts, silk textiles, stone objects, and more. H. Jedrzejewska et al. [23] in Poland reinforced and protected an Egyptian bronze statue of Amon using Paraloid B-72 (referred to as B72, a polymer composed of 66% methyl methacrylate and 34% ethyl acrylate), endowing the artifact with new historical value. However, acrylic resin also has drawbacks, such as a high film-forming temperature, poor water resistance, and low adhesion, which limit its application in cultural heritage conservation. Therefore, formulation modifications are necessary to achieve better compatibility with artifacts.However, acrylic resin also has drawbacks, such as a high film-forming temperature, poor water resistance, and low adhesion, which limit its application in cultural heritage conservation. Therefore, formulation modifications are necessary to achieve better compatibility with artifacts.

In recent years, the application of composite materials in cultural heritage conservation has become increasingly widespread. By modifying materials through composite formulations, superior properties are imparted to the materials, thereby enhancing the compatibility and compatibility between the protective materials and the cultural artifacts. Gong Decai et al. [24] incorporated a UV absorber (UV-9) into B72 to protect and reinforce the painted decorations on wooden cultural relics, effectively improving their resistance to photoaging. After this chemical protection treatment, there was no powdering or peeling of the decorations, and the colors remained unchanged.Chen Jiachang et al. [25–27] developed a highly permeable acrylate metal complex sol for reinforcing bone, pottery, and lacquered wooden artifacts, and it also shows good results in the in-situ stabilization treatment of "powdery rust" on bronze artifacts.

Nanocellulose is a type of fiber with a one-dimensional structure measuring less than 100 nm in width and serves as the fundamental building block of cellulose. Depending on its size and morphology, cellulose can be categorized into cellulose nanocrystals (CNC), cellulose nanofibers (CNF), and bacterial cellulose (BC), also known as microbial cellulose (MC) [28, 29]. Of these types, CNC and CNF can be produced through relatively straightforward processes. These nanofibers exhibit the core properties of natural cellulose, such as regenerability and biodegradability, along with additional features like high specific surface area, enhanced hydrophilicity, remarkable transparency, excellent mechanical stability, and inherent antimicrobial properties [30]. They provide substantial advantages for high-performance composite materials and demonstrate versatility in diverse sectors, including biology, medicine, the food industry, electronics, and the paper industry.Due to their extensive potential applications across numerous fields, nanofibers are gaining significant attention in both research and industry.

To address these aforementioned issues, we conducted an investigation into reinforcement agents focused on the cuprammonium-nanocellulose system, examining their effects when mixed.Subsequently, we created simulated powdery rust test samples derived from fragile bronze artifacts for use in reinforcement experiments. Moreover, various analytical techniques, such as X-ray diffraction (XRD), scanning electron microscopy (SEM), Raman spectroscopy, and electronic universal testing machines, were employed to assess the fundamental properties of the simulated powdery rust samples, both before and after reinforcement.The key innovation in this study lies in the approach of "Treating copper with copper," whereby materials are subjected to a complex formulation designed to convert powdery rust into structurally compact minerals and, eventually, into stable components of bronzes through complexation with a composite gel system that establishes chemical bonds. Concurrently, a dense and stable protective membrane formed on the surface of the bronzes, effectively isolating the bronze substrate from direct exposure to the external environment, thereby mitigating bronze corrosion

and supporting long-term preservation.In summary, this study presents a novel and effective approach for reinforcing and protecting fragile bronze cultural relics.

Materials and methods

Reagents and materials

The self-prepared cuprammonium solvent of a certain concentration [$Cu(NH_3)_4(H_2O)_2$] was the blue solution. Ammonium hydroxide ($NH_3 \cdot H_2O$, AR), polyethylene glycol 4000 ($HO(CH_2CH_2O)_nH$, AR), and urea ($CO(NH_2)_2$, AR) were purchased from Sinopharm Group Chemical Reagent Co., Ltd. The copper chloride hydroxide ($Cu_2(OH)_3Cl$) used for preparing simulated powdery rust samples was commercially available.

Property characterization of the test samples

A DVM-6 ultra-depth of field microscope (LEICA, Germany) was used for surface morphology observation of the bronze stimulated samples at the magnification of 50–1000×. A Quanta 650 environmental scanning electron microscope (FEI, USA) was employed to characterize the microstructure and composition of bronze stimulated samples. The experimental conditions included high vacuum mode,with a working voltage of 25 kV, secondary electron imaging and backscattered imaging. A D8 Focus X-ray diffractometer (Bruker, Germany) was employed to characterize the phase of bronze stimulated samples. The X-ray diffraction conditions were as follows: the radiation source was $Cu/K\alpha$, the wavelength was 15.4 nm, the tube voltage was 40 kV, the tube current was 100 mA, the scanning speed was 5 $(^\circ)/min$, and the diffractometric range was $5 - 80^\circ$. A 3345 universal material testing machine (Instron, USA) was utilized to test the flexural strength of the bronze prowdery rust samples at the degree of measurement from 0 to 5000 N and the load measurement accuracy of ±0.5%. A Apollo-X energy disperse spectroscopy (EDAX, USA) was applied to perform elemental analysis of the bronze powdery rust samples under the experimental conditions including dot scanning and plane scanning. A CR-400 color difference meter (Konica Minolta, Japan) was utilized under the experimental conditions below: measurement time of 1 s, measurement area of 8 mm, and standard deviation of AE<0.07. A INCIA-REFLEX laser Raman spectrometer (Renishaw, UK) was used under the following experimental conditions: gratings of 1200 l/mm and 1800 l/mm, eyepiece of 20x, CCD probe, power of $0.5 - 50W$, and the excitation light sources of 532, 633 and 785 nm.

Preparation of the nano-cuprammonium fiber hydrosol

Due to hydrogen bond interactions, cellulose nanocrystals (CNC) tend to agglomerate, forming large and non-uniform particles that are difficult to disperse in organic solvents, thereby reducing their infiltration capacity on the surface of corrosion products.To improve the dispersibility of CNC powders in organic solvents and their infiltration capacity on the corrosion product surface, it is essential to process the CNC to reduce its particle size [31]. The CNC samples were initially placed in a 60 °C constant-temperature air blast drying oven for 3 h, then transferred into a nylon ball mill for further processing. A zirconia milling medium with a diameter of 5 mm was subsequently added to the ball mill. The mixture was placed in a planetary ball mill for thorough milling at a rotation rate of 800 rpm, with a grinding media-to-material ratio of 0.65, for 8 h to separate the zirconia grinding balls from the powdered material.Following the ball milling process, a portion of the CNC samples underwent additional drying in a 60 °C constant-temperature air blast drying oven for 9 more hours to obtain the nano-scale powders [32–34]. The resulting samples were then subjected to vacuum drying at 60 °C until a constant weight was achieved, after which they were sealed in sample bottles for long-term dry storage [31, 35, 36].

The ball-milled cellulose nanocrystals (CNC) were dispersed in a cuprammonium solvent and subjected to a specific seasoning process. As a result, a nano-cuprammonium fiber hydrosol with a light blue hue was obtained.To determine the optimal concentration of nano-cuprammonium fiber hydrosol for reinforcing powdery rust, we prepared nano-cuprammonium fiber hydrosols at concentrations of 0.5, 1.5, 2.5, and 3.5 mol/L for testing in our experiments [37–39].

Preparation of fragile bronze powdery rust simulated samples

Characterization of ancient bronze artifacts with powdery corrosion rust

(1) Sample information

Four typical bronze relics with characteristic powdery rust disease were selected from the bronze relics sample library. Among them, G1 and P1 are bronze weapon and bronze plate from the Warring States period, respectively; T1 is a bronze mirror from the Han Dynasty; Z1 is a bronze wine cup from the Tang Dynasty. The corrosion product composition and powdery rust morphology of the samples are diverse and typical, demonstrating a certain representativeness. Details of the samples are shown in Table 1.

Table 1 Ancient bronze artifacts powdery rust analysis sample information table

Serial Number	Sample ID	Artifact Name	Period	Original ID
1	G1	Bronze weapon	Warring states	HXXM9:75
2	P1	Bronze plate	Warring states	HXXM9:37
3	T1	Bronze mirror	Han dynasty	2022XHCTM00355
4	Z1	Bronze wine cup	Tang dynasty	2023T15M0043

(2) Morphological characterization analysis

The artifacts G1, P1, T1, and Z1 were successively observed under a scanning electron microscope (SEM) and a digital microscope with high depth of field to examine their surface corrosion features.

(3) Elemental composition analysis

SEM-EDS was employed to detect the surface of the fragile bronze artifacts G1, P1, T1, and Z1 for their powdery rust. Based on the morphological observations, the energy spectrum was used for in-depth quantitative analysis of the elemental composition and percentage differences of the powdery rust on the surface of the bronze artifacts with different morphological characteristics.

(4) Constituent analysis

The surface corrosion products of the artifacts were analyzed using X-ray diffraction (XRD) and Raman spectroscopy. By combining the results of the energy spectrum composition analysis, the phase composition of the powdery rust was further determined qualitatively and quantitatively.

(5) Density and hardness testing

The density of the four powdery rust bronze artifact samples was measured using an electronic densimeter. Additionally, the Vickers hardness of the powdery rust areas on the surface of each artifact was measured using a microhardness tester. Multiple measurements were taken in situ, and the average value was obtained.

Sample G1, a fragment of a bronze weapon from the Warring States period, had a density of 4.32 g/cm^3 and a hardness of 168.5 HV. Under scanning electron microscopy (SEM), the surface of sample G1 exhibited dispersed clusters of powdery rust corrosion products, primarily dark green, interspersed with white and dark gray particles (Fig. 1b). The corrosion products appeared layered and loosely distributed on the surface. Numerous surface pores were observed under SEM (Fig. 1c). Based on X-ray diffraction (XRD) results (Fig. 3) and Raman spectroscopy (Fig. 4), the main components of the powdery rust corrosion products were identified as atacamite ($Cu_2(OH)_3Cl$), malachite ($CuCO_3{\cdot}Cu(OH)_2$), and azurite ($2CuCO_3{\cdot}Cu(OH)_2$).

Sample P1, a bronze food plate from the Warring States period, had a density of 3.18 g/cm^3 and a hardness of 152.3 HV. The corrosion products exhibited a complex morphology. Under super-depth microscopy, the surface appeared predominantly green, with some yellow and white particles interspersed (Fig. 1e). The corrosion products appeared compact and layered. Scanning electron microscopy revealed large blocks of corrosion layers with some structural cracking. XRD results (Fig. 3) and

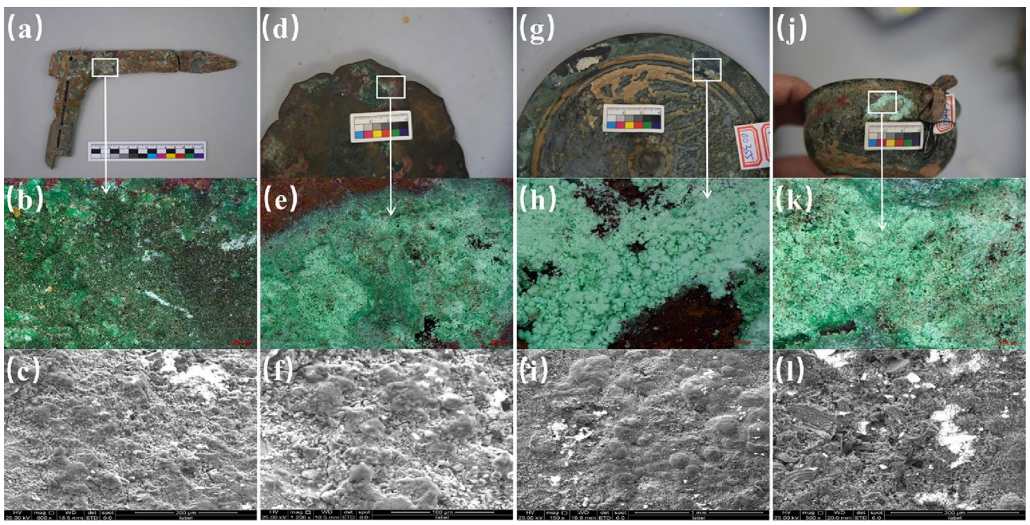

Fig. 1 Corrosion morphological characteristics of powdey rust on cultural relic samples (**a,d,g,j** The surface morphology of powdey rust on cultural relic samples; **b,e,h,k** The ultra-depth of field microscopic photographs of powdey rust on cultural relic samples; **c,f,i,l** The environmental scanning electron microscopy photographs of powdey rust on cultural relic samples)

Raman spectroscopy (Fig. 4) confirmed the presence of paratacamite ($Cu_2(OH)_3Cl$), azurite ($2CuCO_3{\cdot}Cu(OH)_2$), and a small amount of cuprite (Cu_2O) on the surface.

Sample T1, a Han Dynasty bronze mirror, had a density of 3.26 g/cm^3 and a hardness of 89.3 HV. Under super-depth microscopy, the surface exhibited clustered powdery rust corrosion products with predominantly green rust and white particles (Fig. 1h). Scanning electron microscopy revealed a diffusion trend of the corrosion products towards the surrounding area (Fig. 1i). The main component of the surface rust corrosion product was identified as atacamite ($Cu_2(OH)_3Cl$), with traces of cuprous chloride (CuCl) and malachite ($2CuCO_3{\cdot}Cu(OH)_2$).

Sample Z1, a Tang Dynasty bronze wine cup, had a density of 2.39 g/cm^3 and a hardness of 119.4 HV. Among the four samples, Z1 exhibited the most severe powder rust corrosion. The surface appeared porous, loose, and powdery, with white-green rust corrosion products and visible cracks and holes under both super-depth microscopy and scanning electron microscopy. XRD results (Fig. 3) and Raman spectroscopy (Fig. 4) confirmed the presence of malachite ($CuCO_3{\cdot}Cu(OH)_2$), atacamite ($Cu_2(OH)_3Cl$), and some cuprite (Cu_2O) on the surface.

In summary, the primary characteristic of "powdery rust" bronze artifacts is the dense distribution of dispersed or clustered corrosion products on the surface. Although the distribution patterns of these two types of "powdery rust" may differ, they both exhibit strong diffusion characteristics and can be "activated" in suitable environments, leading to the pulverization and eventual disintegration of the bronze artifacts. The main component of powdery rust is copper chloride ($Cu_2(OH)_3Cl$). The rust corrosion products are distributed in layers, uneven in thickness, rough, and fragile, often accompanied by surface cracking, swelling, crack formation, and hole formation. Additionally, "powdery rust" bronze artifacts have a density less than 4 g/cm^3 (the original density of bronze artifacts being 8.56–9.0 g/cm^3), and their Vickers hardness decreases linearly with the degree of corrosion (Fig. 5). The low copper content and high chlorine content in "powdery rust" bronze artifacts may be attributed to the corrosion behavior of cupric chloride compounds, leading to the loss of copper metal (Fig. 2).

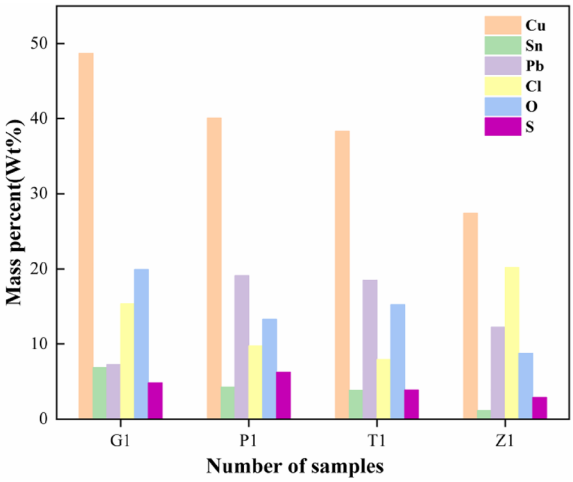

Fig. 2 Elemental composition of powdery rust on cultural relic sample surfaces

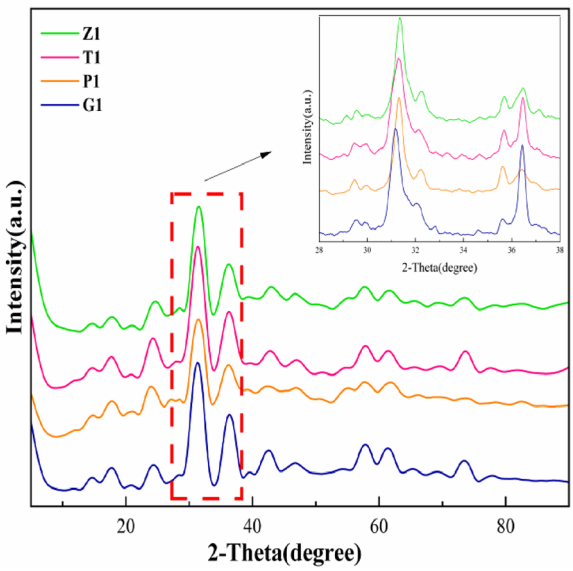

Fig. 3 XRD spectra of powdered rust on cultural relic sample surfaces

Comparison between simulated powdery rust samples and real archaeological bronze artifacts

The simulated powdery rust samples of fragile bronze artifacts should closely resemble the real archaeological artifacts in terms of various characteristics and parameters. Through the analysis of the main features of typical powdery rust bronze artifacts in the previous section, severe corrosion of the alloy matrix is the most obvious characteristic of "powdery rust" bronze artifacts. Therefore, the simulated samples prepared artificially are pressed from compound powders without any alloy matrix. In terms of composition and content, the main components of fragile bronze artifacts include tin dioxide, basic copper carbonate, basic lead carbonate, etc. Therefore, analytical pure tin dioxide, basic copper carbonate, and basic lead carbonate are used as raw materials for the simulated samples. The average surface element content of the four "powdery rust" bronze artifact samples tested is approximately: Sn 48.21%, Cu 10.36%, Pb 6.29%

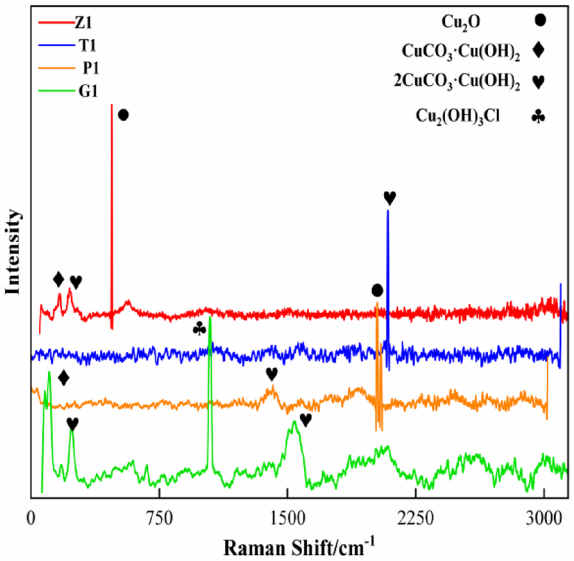

Fig. 4 Raman spectroscopy of powdery rust on cultural relic Sample surfaces

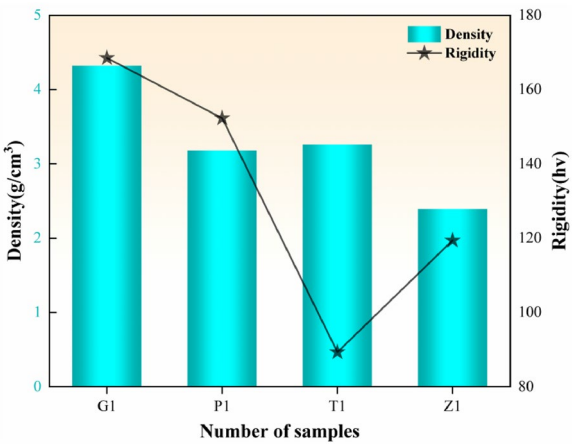

Fig. 5 Average density and hardness of powdery rust on cultural relic samples

(Sn:Cu:Pb≈6:3:1); according to XRF fluorescence spectrum analysis, the main element content of the simulated powdery rust samples is approximately: Sn 49.96%, Cu 15.52%, Pb 9.01%, which is similar to the real archaeological artifact samples. In terms of physical properties, the density of the artifact samples is approximately 2.08–4.59 g/cm^3, and the hardness of the powdery rust corrosion products is approximately 12.3–197.6 HV. After measurement by electronic densimeter and microhardness tester, the density of the simulated powder rust samples is approximately 3.53 g/cm^3, with an average hardness of 22.4 HV, which is similar to the real artifact samples and meets the experimental requirements.

A small amount of menthol was added during the preparation of the simulated samples, which, after heating and volatilization, makes the structure more porous. The surface and cross-section of the simulated samples were observed using a scanning electron microscope, and compared with a typical powdery rust bronze artifact fragment unearthed from Hangzhou, Zhejiang Province. The surface of the unearthed bronze artifact samples is light green, with yellow particles attached to the surface, and numerous pores and cracks; the surface of the simulated samples is also light green, with white lead carbonate particles interspersed, and numerous pores can be observed (Fig. 6c, d). The cross-sections of both the real bronze artifact sample and the simulated sample appear light green under the microscope, with a loose and porous structure, interspersed with a large amount of a large amount of white and green substances (Fig. 6e, f). Overall, the artificially prepared simulated powdery rust samples closely resemble the real powdery rust bronze artifacts in terms of composition, physical properties, and appearance, effectively reflecting the powdery rust corrosion characteristics of real artifacts.

Preparation of fragile bronze powdery rust samples

Weigh tin dioxide, basic copper carbonate, and basic lead carbonate in a ratio of 6:3:1 using a precision balance to

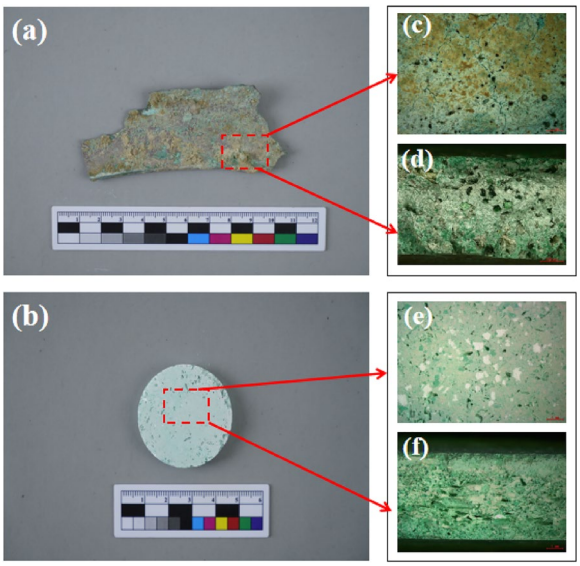

Fig. 6 Comparative ultra-depth of field microscope images of simulated bronze powdery rust samples and the authentic cultural relic sample. **a** image showing the surface of the authentic cultural relic; **b** image showing the surface of the simulated samples; **c** image of the surface of the authentic cultural relic; **d** image of the cross-section of the simulated samples; **e** image showing the surface of the powdery rust simulated test specimen; **f** image of the cross-section of powdery rust simulated samples)

prepare a total of 20 g of raw materials for the simulated sample. Place the raw materials in an agate mortar and grind them clockwise and counterclockwise for several rounds until evenly mixed. After uniform mixing, fill the mixture into the mold. Use an electric press machine to press the mixture at a pressure of 10 MPa into a round cake-shaped sample with a diameter of 40 mm and a thickness of 5 mm (Fig. 7). Place the pressed samples in a vacuum drying oven at 60 °C for 6 h. After the solvent has evaporated sufficiently, leave the samples in a cool place for 48 h [40, 41].

Reinforced treatment of the simulated bronze powdery rust samples

A specific amount of nano-cuprammonium fiber hydrosol reinforcer was used to reinforce the powdery rust samples through instillation with a rubber dropper and even application with a cotton swab. Subsequently, the powdery rust test samples were reinforced at concentration gradients of 0.5, 1.5, 2.5 and 3.5 mol/L. Thereafter, the low concentration reinforcer was utilized for secondary infiltration reinforcement of the fragile powdery rust samples. The reinforcement process was completed once the mass of the simulated samples became constant. Afterwards, the simulated samples were dried in the 60°C constant-temperature air blast drying oven to constant weight, and renumbered for later use (Fig. 8).

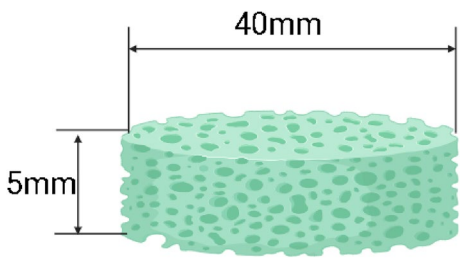

Fig. 7 Structural diagram of simulated powdery rust samples

Characterization methods of the reinforcement effect

Morphology characterization analysis

A DVM-6 ultra-depth of field microscope (LEICA, Germany) was used to observe the surface morphology of the bronze powder rust test specimen at the magnification of 50–1000×. A Quanta 650 environmental scanning electron microscope (FEI, USA) was employed to characterize the microstructure and composition of bronze test samples.

Flexural load test

The Instron 3345 universal material testing machine was utilized to test the mechanical strength of the bronze S powdery rust specimen. The test parameters were shown below: sampling rate (pts/sacs), 10.000; humidity (%), 50; beam speed (mm/min), 25.0000; and temperature, 25 °C. The flexural loads of the bronze powdery rust samples before and after reinforcement were tested.

Mass change fraction test

During this test, the change in the mass of bronze powdery rust samples before and after reinforcement was

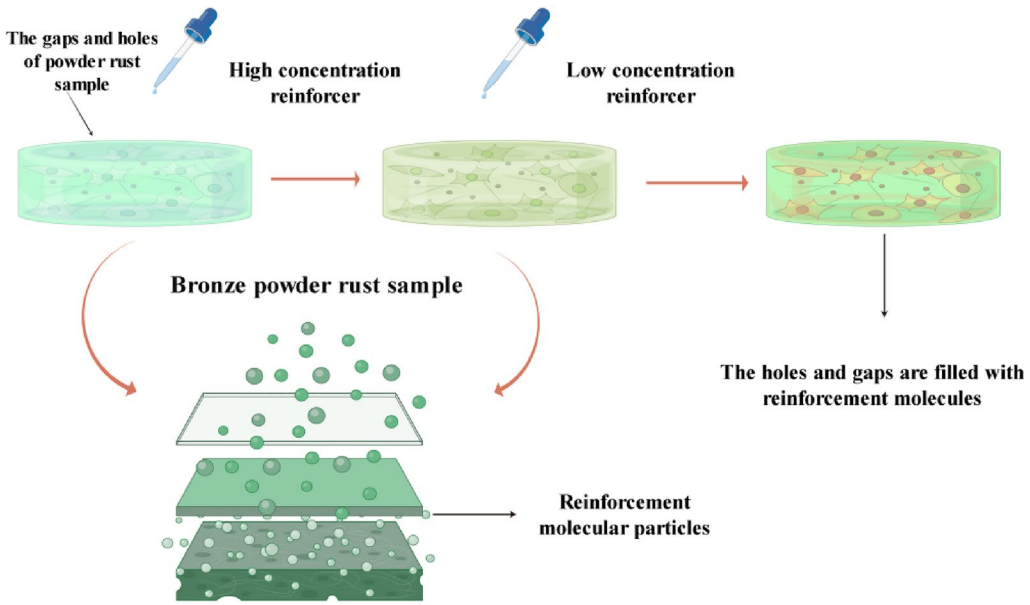

Fig. 8 Reinforcement mechanism diagram for the bronze simulated powdery rust samples based on the nano-cuprammonium fiber reinforcer

calculated to reflect the reinforcement effect of the nano-cuprammonium fiber reinforcer. The change in sample mass was measured with the BSA124S precision electronic balance (SARTORIUS, Germany; measuring range, 0–120 g; precision, 0.1 mg). The formula below was used to calculate the mass growth rate ΔM.

$$\Delta M = \frac{m_1 - m_0}{m_0} \times 100\%. \quad (1)$$

where ΔM is the mass growth rate of the powdery rust samples before and after reinforcement, m_0 represents the mass of the powdery rust samples before reinforcement, while m_1 indicates the mass of the powdery rust samples after reinforcement.

Measurement of color change of the powdery samples

Color difference is a crucial index that can reflect the impact of reinforcement materials on the appearance of cultural relics. The color difference value of the powdery rust samples was measured using a color difference meter to determine the change in test samples color before and after reinforcement with the reinforcement material. The change in the appearance of powdery rust test specimen before and after reinforcement is shown below:

$$\Delta E = \sqrt{\Delta L^2 + \Delta a^2 + \Delta b^2}. \quad (2)$$

where Δ indicates color difference, L stands for the brightness value, a represents the yellow-green value, and b is the yellow-blue value.

Accelerated aging of simulated powdery rust samples

Resistance to aging refers to the ability of materials to withstand aging effects. Aging tests are an important part of testing the performance of materials used in cultural relic preservation and help understand their aging behaviour. Generally, light, temperature, and humidity are considered important factors affecting the preservation of museum collections.

Dry heat accelerated aging experiment

The simulated powdery rust samples,treated with penetration reinforcement were placed in a GDW-50 L high and low temperature aging test chamber for accelerated aging treatment. The aging temperature was set at 110 °C and an aging time at 72 h.

Humid and heat accelerated aging experiment

Artificial humid and heat aging tests were conducted to evaluate the weather resistance and stability of the reinforcement materials. The simulated powdery rust samples, treated with penetration reinforcement were placed in a GDW-50 L high and low temperature aging test chamber for accelerated aging treatment.The aging temperature was set at 70 °C, the relative humidity of 85%, and the aging time at 72 h. Observations were made for phenomena such as cracking or peeling of the samples.

Itraviolet accelerated aging experiment

The ultraviolet accelerated aging experiment utilized a colorimeter to measure the color difference value Δ before and after UV aging. The test conditions of the UV aging chamber referred to relevant research on the theoretical limit of UV intensity. The UVB313-type ultraviolet aging chamber was selected for accelerated aging treatment, with an irradiance of 0.68 W/m^2. The aging temperature was set at 60 °C, and the total UV aging time was 72 h. A super depth of field microscope was used to observe the morphology of the samples before and after UV aging.

Results and analysis

Morphologic analysis

Figure 9 illustrates the environmental scanning electron microscopy (ESEM) images of bronze powdery rust samples, both before and after reinforcement treatment Fig. 9a shows the microstructure of powdery rust samples after reinforcement, while Fig 9b–e depict the microstructural changes in bronze powdery rust samples following reinforcement with reinforcers at concentrations of 0.5, 1.5, 2.5, and 3.5 mol/L, respectively.

As illustrated in Fig. 9a and b, the powdery rust samples that had not undergone reinforcement treatment exhibited a loose structure with numerous holes and gaps, and these holes were both large in size and unevenly distributed. According to the ultra-depth of field image (Fig. 10a), the mineral particles were loosely stacked, creating pores of varying sizes As the concentration of the reinforcer increased, the reinforcement strength also rose, leading to a gradual filling of the pores and gaps in the powdery rust samples. At a reinforcer concentration of 2.5 mol/L, the optimal filling effect on pores and gaps was achieved, as evidenced by a smooth surface on the samples (Figs. 9d, 10d). Additionally, part of the reinforcer adhered to the surface of the mineral particles, binding micro-mineral particles and some impurities together, resulting in a dense and compact membrane structure on the surface of the powdery rust samples, effectively isolating them from the external environment[11]. When the reinforcer concentration exceeded 2.5 mol/L, noticeable accumulation of large reinforcer particles was observed on the surface of the samples (Figs. 9e, 10e).This occurred because the holes and gaps in the samples were filled to a saturation state, reducing the infiltration capacity of any additional

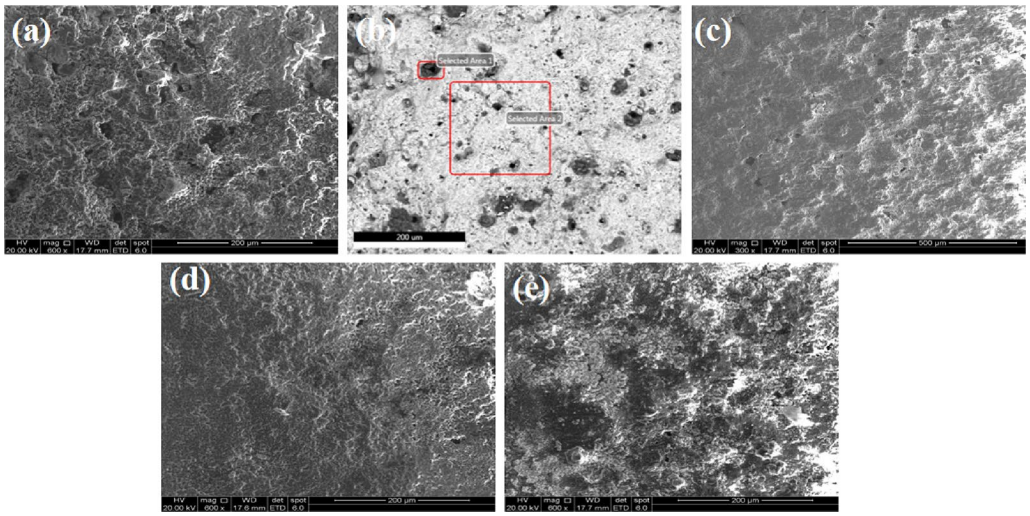

Fig. 9 The environmental scanning electron microscopy photographs of the bronze powdery rust samples before and after reinforcement. **a** untreated samples; **b** samples reinforced with 0.5 mol/L reinforcer; **c** samples reinforced with 1.5 mol/L reinforcer; **d** samples reinforced with 2.5 mol/L reinforcer; **e** samples reinforced with 3.5 mol/L reinforcer

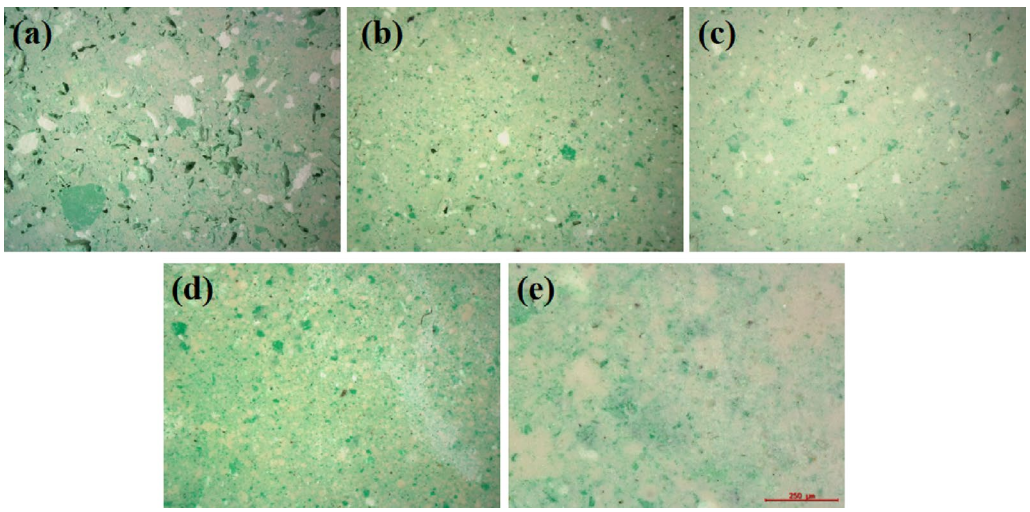

Fig. 10 The ultra-depth of field microscopic photographs of the bronze powdery rust samples before and after reinforcement. **a** untreated samples; **b** simulated samples reinforced with 0.5 mol/L reinforcer; **c** simulated samples reinforced with 1.5 mol/L reinforcer; **d** simulated samples reinforced with 2.5 mol/L reinforcer; **e** simulated samples reinforced with 3.5 mol/L reinforcer

reinforcer, leading to reinforcement material accumulating on the surface of the powdery rust samples.

Mechanical strength analysis

Figure 11 illustrates the mechanical strength of bronze powdery rust samples following treatment with nano-cuprammonium fiber reinforcer at various concentrations.According to Fig. 6, as the concentration of nano-cuprammonium fiber reinforcer increased, the mechanical strength of the powdery rust samples gradually rose.The highest compressive strength of 89.52 N was achieved at a reinforcer concentration of 2.5 mol/L. Additionally, the mechanical strength of the powdery rust samples increased by an average of 77.59% after reinforcement, compared to their strength before treatment. Furthermore, the moderate length of the error bars at this concentration indicated that the error was relatively small, suggesting the experimental data were more stable, less variable, and consequently more reliable. However, when the reinforcer concentration exceeded 2.5 mol/L, the mechanical strength began to decline.This could be because as the concentration of

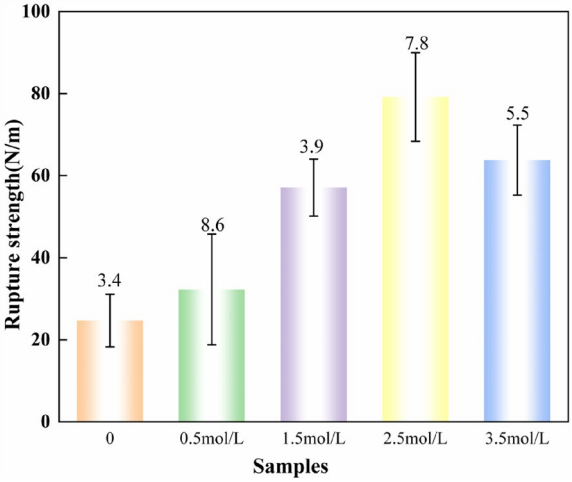

Fig. 11 Impact of reinforcer concentration of the mechanical strength of the powdery rust bronze test specimen

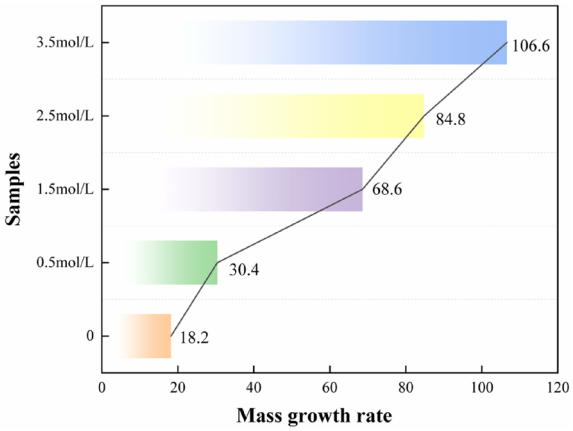

Fig. 12 Impact of reinforcer concentration on the mass growth rate of powdery rust test specimen

the nano-cuprammonium fiber reinforcer increased, the nanocellulose content in the powdery rust samples became excessively high. This led to the holes and gaps in the powdery rust samples being filled to a saturation state, causing nanocellulose to accumulate on the surface, thereby hindering further reinforcer infiltration and, in turn, impacting the surface mechanical strength. Flexural load experimental data indicated that the mechanical strength of the powdery rust samples increased significantly after reinforcement.The scanning electron microscopy microstructure image (Fig. 9) shows that the nano-cuprammonium fiber hydrosol reinforcer filled the holes and gaps in the powdery rust samples, leading to increased compactness.These two factors contributed to the enhanced mechanical strength of the powdery rust samples.

Mass growth rate of bronze powdery rust samples before and after reinforcement

The retention of the reinforcer in bronze powdery rust samples can be measured by the rate of mass increase. A higher rate of mass increase indicates a greater retention of reinforcement material in the powdery rust samples and suggests a more effective reinforcement process; conversely, a lower rate indicates a weaker reinforcement effect [42].

As illustrated in Fig. 12, as the concentration of nano-cuprammonium fiber reinforcer increased, the mass growth rate of the powdery rust samples exhibited a continuous upward trend, suggesting that the reinforcement effect improved as the reinforcer concentration increased. The cohesion among powdery rust samples increased, resulting in enhanced reinforcement effects.When the reinforcer concentration reached 3.5 mol/L, the mass growth rate of the powdery rust test specimens peaked at 106.6%. However, the reinforcement effect at this concentration was not optimal. The high mass growth rate at this concentration could be attributed to the deposition of reinforcer on the surface of the test samples due to its excessively high concentration [43, 44]. This result aligns with the earlier observation of changes in the mechanical strength of the powdery rust samples.

Change in the appearance of bronze powdery rust test specimen before and after reinforcement

The variation in the appearance of bronze powdery rust samples, both before and after reinforcement, was assessed through color difference (Fig. 13). Upon analysis, it was discovered that the color difference Δ for powdery rust samples post-reinforcement was under 4.0 at a reinforcer concentration of less than 1.5 mol/L, falling beneath the standard threshold of 5.0 [38, 45]. This finding indicates that at lower concentrations of reinforcer, reinforcement protection does not alter the appearance of powdery rust samples. Moreover, the shortest error bar length was observed at a reinforcer concentration of 1.5 mol/L, suggesting minimal error and indicating that the experimental data were more stable, less variable, and more reliable. Excessively high concentrations of reinforcer were found to partially affect the appearance of powdery rust samples.The findings suggest that the permeability of reinforcement material is partially correlated with the concentration of the reinforcer.Excessively high reinforcement material concentrations generally reduce the permeability of the reinforcement material. Consequently, the reinforcement material tends to deposit on the surface of the reinforced substrate, potentially altering its original appearance. Conversely, repeated

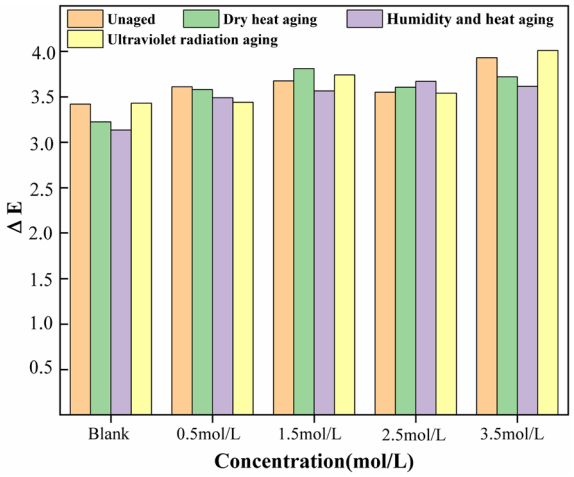

Fig. 13 Color change before and after reinforcement of powdery rust simulated samples on bronze artifacts

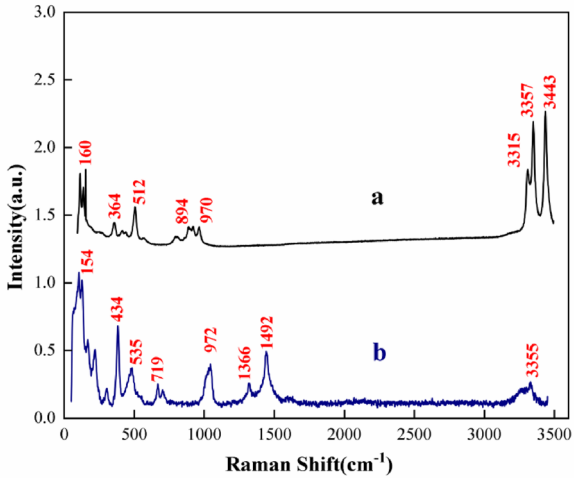

Fig. 14 Raman laser spectra of bronze powdery rust test specimen before and after reinforcement. **a** Untreated simulated powdery rust samples; **b** reinforced simulated powdery rust samples

penetration at low concentrations can significantly enhance the permeability of the reinforcement material. This leads to maximal dispersion of the reinforcement material into the core of the reinforced substance, with only minimal deposition on the matrix surface, thereby maintaining the original appearance.

Phase composition analysis

Figure 15 presents the X-ray diffraction spectra of powdery rust samples before and after reinforcement. After analysis, it was determined that the untreated powdery rust samples primarily contained atacamite ($Cu_2(OH)_3Cl$), with characteristic 2θ diffraction peaks at 9.52°, 12.30°, 28.47°, 40.08°, and 31.12°. The X-ray diffraction spectra of the reinforced terracotta test specimen exhibited 2θ characteristic diffraction peaks at 16.88°, 30.16°, 34.75°, 38.92°, 39.02°, and 46.83° [46]. The intensity of the diffraction peaks increased after reinforcement in a manner that correlated with the concentration of the reinforcer. Certain diffraction peaks vanished, suggesting the emergence of a new phase in the powdery rust test specimen after reinforcement with nano-cuprammonium fiber. Further analysis revealed that the primary component of the new phase was malachite ($CuCO_3{\cdot}Cu(OH)_2$). This compound was produced by the reaction between nano-cuprammonium fiber at different concentrations and $Cu_2(OH)_3Cl$, but with varying yields depending on the concentration [46, 47].

Figure 14a shows the laser Raman spectra of powdery rust samples prior to reinforcer treatment. The Raman spectra exhibited characteristic peaks closely matching the standard Raman peaks for atacamite ($Cu_2(OH)_3Cl$) at 149, 358, 411, 449, 512, 896, 930, 3329, 3349, and 3433 cm^{-1} [48–51], indicating that its primary component was atacamite. Figure 14b displays the laser Raman spectra of powdery rust test specimen after reinforcer treatment. After reinforcement, a new characteristic peak appeared on the spectra of powdery rust samples, suggesting the formation of a new phase. Additionally, the characteristic peaks were close to the standard Raman peaks for malachite ($CuCO_3{\cdot}Cu(OH)_2$) at 154, 180, 219, 434, 538, 1367, 1462, 1493, and 3378 cm^{-1} [52–54], indicating that malachite was the primary component.The Raman spectra post-reinforcement still exhibited a characteristic peak corresponding to atacamite, albeit with significantly reduced intensity, aligning with the results of the X-ray diffraction analysis (Fig. 15).

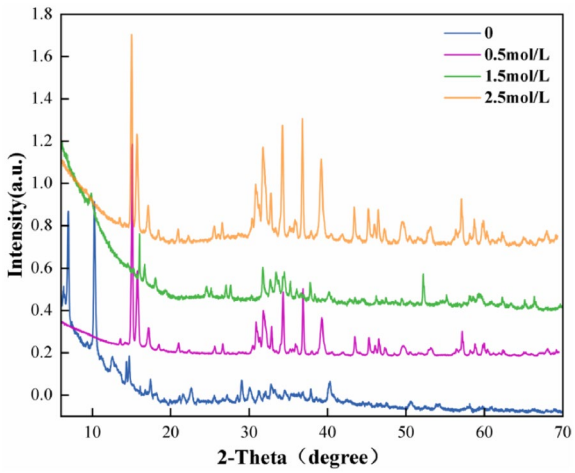

Fig. 15 XRD spectra of the bronze powdery rust test specimen before and after reinforcement

Effect of different concentrations reinforcement solvent on the aging resistance of simulated powdery rust samples

The reinforced simulated powdery rust samples underwent dry heat, humid heat, and ultraviolet aging experiments, and the color changes of the simulated samples were observed, as shown in Figs. 13 and 16. It was observed that the samples treated with nano-cuprammonium fiber reinforcement solvent showed almost no color change, but after dry heat, wet heat, and ultraviolet aging, the colors of the samples changed. As the concentration of the reinforcement agent increased, the color change became more pronounced,with surface yellowing, darkening, and cracking observed, affecting the original appearance of the simulated samples. Especially for samples treated with a 3.5mol/L reinforcement agent, the color difference after ultraviolet aging was the greatest, and the surface color of the samples changed significantly.This may be because the cellulose nanocrystals oxidized under continuous high-temperature conditions, resulting in surface yellowing, darkening, and deepening of color.

Concerning the longevity of the reinforcement material, after treatment with a 2.5 mol/L nano-cuprammonium fiber reinforcement solvent, the simulated powdery rust samples exhibited swelling on the surface after 48 h of dry heat aging, and chunky peeling after 60 h of dry heat aging. After 32 h of humid heat aging, there was no noticeable change on the surface of the samples, but the surface of the blank group samples appeared yellowish and peeled off. After 65 h of ultraviolet aging, the surfaces of the samples exhibited noticeable pores, darkened color, while the surfaces of the blank group samples developed black spots with significant color changes. Because nanocellulose is a non-toxic, antibacterial, and biodegradable environmentally friendly material, the nano-cuprammonium fiber reinforcement solvent is reversible, causing minimal damage to the substrate of cultural relics.

The experimental results indicate that the samples treated with a 2.5 mol/L nano-cuprammonium fiber reinforcement solvent exhibited minimal color difference and optimal aging resistance after dry heat, humid heat, and ultraviolet aging. At this concentration, the permeability effect of the reinforcement agent also reached its optimal state.

In this study, scanning electron microscopy (SEM), Raman spectroscopy, X-ray diffraction (XRD), color difference, mass growth rate, and mechanical strength tests were employed to assess the filling capacity and reinforcement efficacy of the protective material.All these analytical techniques confirmed that the protective material exhibited a favorable reinforcement effect. Consequently, this reinforcement method demonstrated effective protective qualities.To further explore the reinforcement effect of nano-cuprammonium reinforcement material on authentic cultural relics, we chose a Tang Dynasty bronze mirror with characteristic powdery rust disease as the subject of reinforcement.

After thorough examination, it was found that the mirror exhibited significant localized corrosion (Fig. 18a, b). The white-green corrosion byproduct was interspersed with various impurities. The surface contained numerous holes, with their number steadily increasing. The powdery rust exhibited a punctiform distribution pattern. Under specific conditions, the powdery rust progressively expanded inward and outward, demonstrating a diffusive

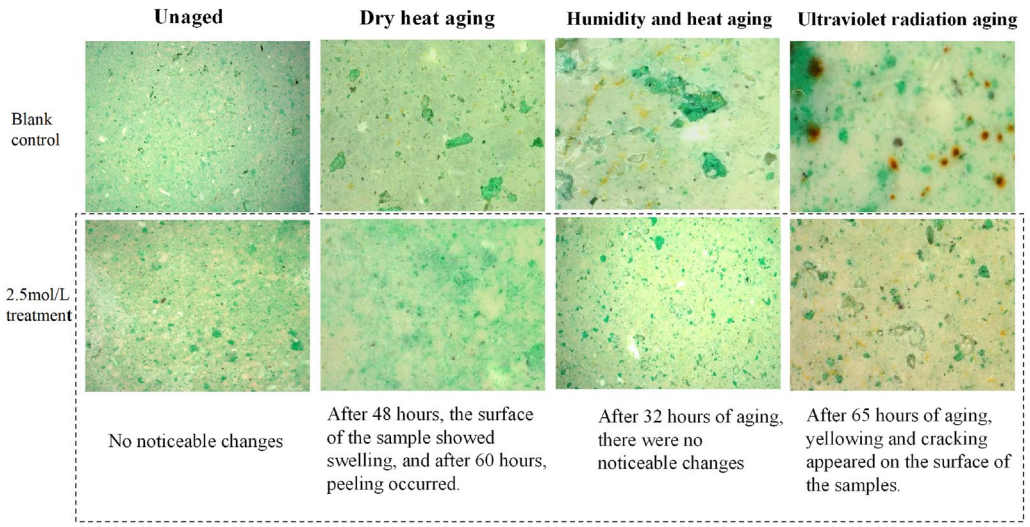

Fig. 16 Aging before and after treatment with nano-cuprammonium fiber reinforcement solvent powdery rust simulated samples

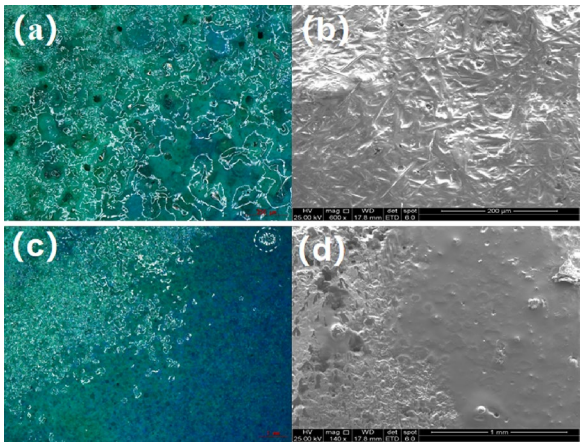

Fig. 17 The ultra-depth of field microscopic photographs (**a**, **c**) and the environmental scanning electron microscopy photographs (**b**, **d**) of the bronze powdery rust samples after reinforcement

distribution pattern [55]. The observed corrosion pattern was consistent with that typically seen in open powdery rust [56].

Figure 18 depicts a bronze mirror from the Tang Dynasty exhibiting characteristic features of powdery rust disease. Through thorough examination and analysis, it was found that the mirror had undergone severe localized corrosion. The white-green corrosion product was intermixed with various impurities, and the surface contained numerous holes, with the number of holes progressively increasing. The powdery rust exhibited a punctiform distribution under certain conditions. Furthermore, the rust gradually expanded inward and toward the periphery, exhibiting a diffusion pattern [55, 56].

Following reinforcement with the nano-cuprammonium fiber reinforcer, the Tang Dynasty bronze mirror was stored in an open environment for over one year. The morphological changes in the bronze mirror after reinforcement are depicted in Fig. 18c, d. Prior to reinforcement, the rusted areas of the bronze mirror were loose and porous, with powdery rust diffusing outward toward the edges. After reinforcement with a 2.5 /L nano-cuprammonium fiber reinforcer via surface instillation and smearing, the holes and gaps in the corrosion product on the mirror's surface were effectively filled. The surface structure became denser and more compact. Additionally, the overall strength of the rusted area was significantly enhanced.The aggressive diffusion and expansion of powdery rust significantly decreased, allowing the mirror to be preserved stably for an extended period.

Conclusions

In conclusion, this study used a hydrosol of nanocellulose whiskers in a cuprammonium solvent as a reinforcer for fragile bronze artifacts afflicted by powdery rust, yielding a favorable reinforcement effect. The key findings from this research are summarized as follows:

1. When the concentration of nano-cuprammonium reinforcer was set at 2.5/L, the optimal reinforcement effect on powdery rust test specimens was achieved. The mechanical strength increased by an average of 77.59%.The mass growth rate reached 84.8%, while the color difference ΔE remained below 4.0, meeting the standards for cultural relics protection.Thus, the principle of minimal intervention in heritage objects was upheld.
2. The cuprammonium solvent formed a coordinated complex with copper ions in the minerals. This process enhanced the bonding strength between mineral particles, leading to the partial conversion of the powdery rust in fragile bronzes into smooth and compact minerals (Fig. 17c, d). The minerals formed

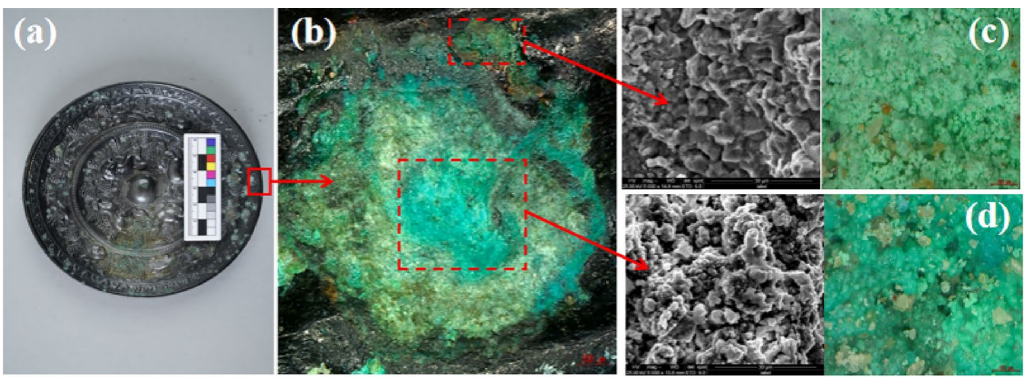

Fig. 18 Surface morphology of the bronze mirror of Tang Dynasty unearthed through archaeological excavation before and after reinforcement (**a**, **c** before reinforcement; **b**, **d** after reinforcement)

after reinforcement acted as stable components of the bronzes.

3. The nanocellulose whiskers in the reinforcer were able to form chemical bonds with chloride in the powdery rust test specimen, effectively filling the holes and gaps within the bronze powdery rust. Additionally, this process contributed to the formation of a compact and stable protective membrane on the test specimen's surface, isolating the bronze matrix from direct contact with the external environment, thereby relatively delaying the corrosion of bronze (Fig. 17a, b). This achieved the in situ reinforcement transformation of fragile bronze powdery rust, thereby significantly enhancing the stability and toughness of fragile bronzes, allowing them to be effectively and stably preserved.

Our future work will involve measuring the cross-sectional corrosion profile of samples before and after treatment with nano-cuprammonium fiber material, with the goal of achieving effective reinforcement for bronze artifacts with varying alloy compositions.This is important because a high degree of adaptability to surface roughness is crucial for meeting the needs of curators working on archaeological bronze artifacts with complex decorative patterns.

Abbreviations

SEM	Scanning electron microscopy
EDX	Energy dispersive X-ray spectrometer
XRD	X-ray difraction
Raman	Raman laser spectrum
CNC	Nanocellulose

Acknowledgements
Not applicable.

Author contributions
We thank the first author, Master Jinlong Tan, for his contributions to this article, including conducting experiments, analyzing data, and writing sections. We also thank Dr. Jiachang Chen, the corresponding author, for his contributions to this article, including revising the manuscript and analyzing the experimental results. Additionally, we thank the third author, Mr. Xinzhan Cui, for providing access to the instruments and equipment. Finally, we are grateful to the National Key Research and Development Program of China for financial support.

Funding
The authors acknowledge the fnancial support provided by National Key Research and Development Project (2020YFC1522000).

Data availability
All data generated or analyzed during this study are included in this published article.

Declarations

Competing interests
The authors declare that there are no competing interest regarding the publication of this paper.

Author details
[1]Zhengzhou University, Zhenzhou 450002, China. [2]China Academy of Cultural Heritage, Beijing 100029, China. [3]Henan Provincial Institute of Cultural Relics and Archaeology, Zhenzhou 450000, China.

Received: 4 January 2024 Accepted: 27 May 2024
Published online: 26 July 2024

References

1. Song M. Conservation of bronzes excavated from the tomb of cai hou. Museum. 1984;1:68–72.
2. Panagopoulou A, Karydas A, Banou E. Chemical analysis of bronze votives from the minoan peak sanctuary at ayios yeoryios sto vouno, kythera. J Archaeol Sci Rep. 2024;53: 104314.
3. Li H, Li W, Li P, Yang P, Zhang T, Cheng Y. Influence of citrate/tartrate on chromite crystallization behavior and its potential environmental implications. J Hazard Mater. 2023;443: 130155.
4. Fan CW, Wang C. Study on the mechanism of powdery rust generation in bronze. Chin Sci (Ser B Chem Life Sci Geol). 1991;3:239–45.
5. Mikić D, Ćurković HO, Hosseinpour S. Bronze corrosion protection by long-chain phosphonic acids. Corros Sci. 2022;205: 110445.
6. Wang Y, Wei G, Li Q, Zheng X, Wang D. Provenance of Zhou dynasty bronze vessels unearthed from Zongyang county, Anhui province, China: determined by lead isotopes and trace elements. Herit Sci. 2021;9(97):1–12.
7. Scott DA. Bronze disease: a review of some chemical problems and the role of relative humidity. J Am Instit Conserv. 1990;29(2):193–206.
8. Porcu D, Innocenti S, Galeotti M, Striova J, Dei L, Carretti E, Fontana R. Spectroscopic and morphologic investigation of bronze disease: performance evaluation of portable devices. Heritage. 2022;5(4):3548–61. https://doi.org/10.3390/heritage5040184.
9. Monari G, Galeotti M, Matteini M, Salvadori B, Stifanese R, Traverso P, Vettori S, Letardi P. Protective treatments for copper alloy artworks: preliminary studies of sodium oxalate and limewater effectiveness against bronze disease. Environ Sci Poll Res. 2023;30(10):27441–57.
10. Kwon H. Corrosion behaviors of artificial chloride patina for studying bronze sculpture corrosion in marine environments. Coatings. 2023;13(9):1630.
11. Molina MT, Cano E, Ramírez-Barat B. Protective coatings for metallic heritage conservation: a review. J Cult Herit. 2023;62:99–113. https://doi.org/10.1016/j.culher.2023.05.019.
12. Zhao J. Stability performance of macromolecular cultural relics protective coating materials and their application in the protection of colored relics. Kirkland: Northwest University; 2007.
13. Liangbo L. Research on reinforcement technology of archaeologically unearthed fragile bronzes. Silk Road. 2012;10:19–20.
14. Park H. Conservation of the reliquary from the east pagoda at Gameunsa temple site. Conserv Sci Mus. 2012;13:59–69.
15. Gong X, Hang X, Chen K. Application of atypical acrylics materials in relics protection. Sci Conserv Archaeol. 2013;3:108–17.
16. Wan L. Introduction of the protection and restoration of bronze relics in nanjing museum. Cultural Relics Science and Technology Research Series IV, 2006;26–34
17. Xie X, Huang Q, Long J, Ren Q, Hu W, Liu S. A new monitoring method for metal rust removal states in pulsed laser derusting via acoustic emission techniques. J Mater Process Technol. 2020;275: 116321.
18. Zhao F, Sun M, Tie F, Wu C, Zhang X, Mu X. Inlaid materials and techniques of an ancient Chinese bronze mirror. Eur Phys J Plus. 2020;135(8):666.
19. Jiao R, Sun F, Li J. Application of low-temperature plasma for the removal of copper chloride layers on bronze wares. Herit Sci. 2023;11(1):28.
20. Yu M. Restoration of a bronze crane from the mausoleum of the first Qin emperor. Sci Conserv Archaeol. 2019;1:86–91.
21. Zhang K, Li L, Chen X, Lu C, Ran J. Controlled preparation and properties of acrylic acid epoxy-acrylate composite emulsion for self-crosslinking coatings. J Appl Polymer Sci. 2022;139(1):51441.
22. Presentato A, Armetta F, Spinella A, Chillura Martino DF, Alduina R, Saladino ML. Formulation of mesoporous silica nanoparticles for controlled release of antimicrobials for stone preventive conservation. Front Chem. 2020;8:699.

23. Jedrzejewska H. The conservation of ancient bronzes. Stud Conserv. 1964;9(1):23–31.
24. Gong Decai ZJ. He Weijun: research on protection technology for polychrome paintings without ground layer. Cult Relics Protect Archaeol Sci. 2004;16(1):29–32.
25. Horie V. Materials for conservation. London: Routledge; 2013. https://doi.org/10.4324/9780080940885.
26. Nie Wangyan ZY. Research on organic silicon-acrylic ester emulsion coatings for stone carving protection. Studies in conservation. 2006;9:29–32.
27. Chen X, Wang JC, Chen LL. Research on the reinforced protection of unearthed fragile ceramic relics using acrylate complex sol. Mater Rev. 2015;2:479–82.
28. Chandra N, George J, Narayanankutty SK. Isolation and characterization of cellulose nanofibrils from arecanut husk fibre. Carbohydr Polym. 2016;142:158–66. https://doi.org/10.1016/j.carbpol.2016.01.015.
29. Isogai A. Emerging nanocellulose technologies: recent developments. Adv Mater. 2021;33(28):2000630. https://doi.org/10.1002/adma.202000630.
30. Jonoobi M, Oladi R, Davoudpour Y, Oksman K, Dufresne A, Hamzeh Y, Davoodi R. Different preparation methods and properties of nanostructured cellulose from various natural resources and residues: a review. Cellulose. 2015;22:935–69.
31. Yong Q. Research on the reinforced protection of paper relics based on nanocellulose fibril composite materials. Xi'An: Shaanxi Normal University; 2020.
32. Yan J, Dang G. Theoretical analysis of the optimal parameters of planetary ball mill. Equip Electr Prod Manuf. 1990;3:47–51.
33. Wang C, Li B, Peng X. Stability analysis of nanoparticle suspension. J Appl Foundation Eng Sci. 2003;11(2):167.
34. Yang A, Qiao C, Hou J. Cause and solution of nano-powder agglomeration. Shanxi Chem Ind. 2003;23(1):56.
35. Haafiz MM, Hassan A, Arjmandi R, Marliana M, Fazita MN. Exploring the potentials of nanocellulose whiskers derived from oil palm empty fruit bunch on the development of polylactid acid based green nanocomposites. Polym Polym Comp. 2016;24(9):729–34.
36. Midhun V, Suresh S, Praveen B, Neethikumar R, Rajesh K. Preparation, characterisation and thermal property study of micro/nanocellulose crystals for vacuum insulation panel application. Therm Sci Eng Prog. 2021;25:101045.
37. Nordeng M, Dietrichson S, Karthäuser J. Method to disperse nanocellulose in organic polymer precursors. Google Patents. US Patent 2021;11,186,689
38. Rodrigues JD, Grossi A. Indicators and ratings for the compatibility assessment of conservation actions. J Cult Herit. 2007;8(1):32–43.
39. Sadeghifar H, Filpponen I, Clarke SP, Brougham DF, Argyropoulos DS. Production of cellulose nanocrystals using hydrobromic acid and click reactions on their surface. J Mater Sci. 2011;46:7344–55.
40. Lin X. Properties and selection of pharmaceutical tablet press. Strait Pharm J. 2014;26(02):29–32.
41. Li H. Comparison of feed modes of tablet press and analysis of performances. Mech Electr Inform. 2009;32:35–7.
42. Liu YF, Zhang Y, Wang QM. Research on the reinforced protection of weathered fragile bone relics based on hydroxyapatite materials. J Inorg Mater. 2023;38(11):1345–54.
43. Zamani S, Ghanbari K, Bonyadi S. Electrochemical determination of metformin via a carbon paste electrode modified with an ag nps/cu 2 o/cuo-decorated bacterial nanocellulose composite. Analy Methods. 2023;15(35):4606–14.
44. Tangsatianpan V, Torgbo S, Sukyai P. Release kinetic model and antimicrobial activity of freeze-dried curcumin-loaded bacterial nanocellulose composite. Polym Sci Ser A. 2020;62:218–27.
45. Zhao T, Zhao L, Feng Y, Luo Q, Zhong J, Li Q. Corrosion of ancient chinese bronze fragments from different periods and protective effect of menthol coating. Corros Commun. 2023;12:46–57.
46. Kovalenko E, Podurets K, Murashev M, Glazkov V, Kartashov S, Chichaev I, Kainov SY, Murasheva V, Tereschenko EY, Yatsishina E, et al. X-ray, synchrotron, and neutron imaging of metal artifacts from the Chernaya mogila (black grave) burial mound. Nanotechnol Russia. 2020;15:572–83.
47. Garrido F, Li T. A handheld XRF study of late horizon metal artifacts: implications for technological choices and political intervention in copiapó, northern chile. Archaeol Anthropol Sci. 2017;9:935–42.
48. Pohl M, Pieck A, Hanewinkel C, Otto A. Raman study of formic acid and surface formate adsorbed on cold-deposited copper films. J Raman Spectrosc. 1996;27(11):805–9.
49. Zhang X, Wallinder IO, Leygraf C. Mechanistic studies of corrosion product flaking on copper and copper-based alloys in marine environments. Corros Sci. 2014;85:15–25.
50. Hamilton J, Farmer J, Anderson R. In situ Raman spectroscopy of anodic films formed on copper and silver in sodium hydroxide solution. J Electrochem Soc. 1986;133(4):739.
51. Coccato A, Bersani D, Coudray A, Sanyova J, Moens L, Vandenabeele P. Raman spectroscopy of green minerals and reaction products with an application in cultural heritage research. J Raman Spectrosc. 2016;47(12):1429–43.
52. Saraiva AS, Figueiredo E, Águas H, Silva RJ. Characterisation of archaeological high-tin bronze corrosion structures. Stud Conserv. 2022;67(4):222–36.
53. Frost RL, Weier ML, Williams PA, Leverett P, Kloprogge JT. Raman spectroscopy of the sampleite group of minerals. J Raman Spectrosc. 2007;38(5):574–83.
54. Tirpak J, Tirpakova A, Zabojnik J. Use of discriminant analysis of data from the fluorescence spectometry analysis of archaeological metal artefacts. Statistika. 2017;97(4):33–44.
55. Chen Y, Mai J, Shang Z. Research status and prospect of ancient bronze powder rusts. Corros Prot. 2023;44(1):51–7.
56. Zhou H, Zhu H, Cai L. Comparative study on the composition and morphology of the bronze corrosion structure. Cult Relics Protect Archaeol Sci. 2005;17(3):22–7.

Publisher's Note